Fatigue Crack Path in new generation Al alloys: coupled influence of microstructure and atmosphere environment.

J. Petit[1], C. Sarrazin-Baudoux[1], S. Richard[1] and C. Gasquères[2].

[1]LMPM, UMR CNRS 6617, ENSMA, 86961 Chasseneuil-Futuroscope, France
jean.petit@lmpm.ensma.fr, baudoux@lmpm.ensma.fr
[2] Centre de Recherches Alcan, Voreppe, France

ABSTRACT. The fatigue crack propagation behavior of new generation Al alloys developed for aeronautical applications depends on alloy composition, aging condition and atmosphere environment. The crack path and the growth rate at moderate ΔK and in the near-threshold domain are governed by the slip morphology. In absence of environment assistance, a stage I-like regime with slow growth rates is produced for shareable precipitates or solute cluster structures that promote heterogeneous slip band formation and (111) faceted cracking in Al-Li-Cu alloys and underaged Al-Cu-Mg alloys, in contrast with a ductile transgranular featureless stage II crack path in overaged Al-Cu-Mg. In air, water vapor assistance induces a transgranular stage II regime associated to homogeneous slip generating a flat-facet and step-like features for all materials; an adsorption assisted propagation mechanism is assumed to prevail at moderate ΔK in both Li and Mg bearing materials and in the near-threshold domain for Al-Cu-Mg alloys in contrast to hydrogen assistance for Al-Cu-Li alloys at low growth rates.

Keywords: Aluminum alloys, fatigue crack path, atmosphere assistance, aging condition, slip mechanisms.

INTRODUCTION

Weight saving is a strategic issue in aeronautics reinforced by the dramatic increase in fuel prices. Due to their good specific mechanical properties, aluminum alloys are widely used to answer this issue. New generation aluminum alloys are developed to improve the properties through optimization of microstructures of conventional alloys as for 2024A or 2022 alloys, and through a reduction of the material density by mean of Lithium addition as for 2050 alloy. Damage tolerance properties being of primary importance for aerospace structures, the aim of this paper is a study the fatigue crack propagation resistance of these new generation alloys. During a flight materials used for constitutive parts of aircrafts are confronted to a wide range of temperature depending on climate and altitude, from about 270K to 330K on the ground down to 220K during high altitude cruise, and partial pressure of water vapor varying from 1Pa to 1.7KPa. The objective of this research is to improve characterization and understanding of the coupled influence of microstructure and atmosphere environment on the fatigue crack path and growth rate in a selection of new generation Al alloys by comparing the behavior of Al-Cu-Mg and Al-Cu-Li alloys in ambient and in high vacuum considered as reference inert environment.

BACKGROUND

Following the pioneer work of Dahlberg in 1956 [1] reporting on high strength steel a substantial effect of moisture on fatigue crack growth rate, thorough analyses of the fatigue crack growth rate as a function of environment were performed on Aluminum alloys [2-28], and also on various metals and metallic alloys [29-30]. From this numerous literature, some main characteristics of environmental effect on fatigue crack propagation can be brought out:

i) a detrimental effect of atmosphere water vapor on most of metals and metallic alloys;
ii) a pronounced atmosphere effect at low growth rate, i.e. in the low stress intensity factor range;
iii) a large interrelation between environment and microstructure;
iv) a characteristic influence on fracture surface morphology.

For long cracks in polycrystalline Al alloys as well as for most of the metallic alloys, four propagation regimes have been highlighted [20- 22, 26, 27, 29, 30, and 35] as illustrated in Figure 1:

i) Two intrinsic regimes operative in inert environment as high vacuum:

- The intrinsic stage II which is favored by peakaged and overaged microstructures containing large and semi-coherent or non-coherent precipitates, and by large plastic zone favoring the activation of different slip systems leading to homogeneous deformation and smooth crack path. An intrinsic propagation law has been derived [29, 30] as:

$$da/dN = A/D_0^*[\Delta Keff/E]^4 \quad (1)$$

where A is a dimensionless parameter and D_0^* the critical cumulated displacement.

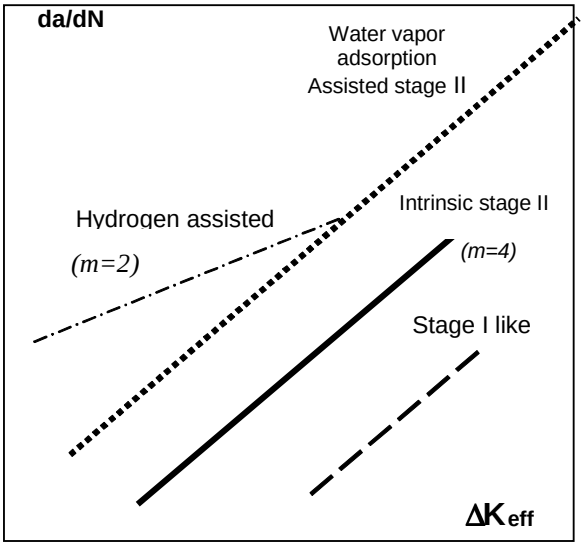

Figure 1: schematic illustration of the four basic crack propagation regimes.

- The crystallographic intrinsic stage I-like propagation is promoted by microstructures containing fine shearable precipitates such as GP zones in underaged Al alloys. The associated deformation is heterogeneously localized within slip bands in each individual grain along the crack front. This leads to highly crystallographic crack propagation associated to tortuous crack path and enhanced roughness of fracture surfaces [20, 29, 30, and 31]. This stage in polycristal is generally characterized by a strong retardation due to the barrier effect of grain boundaries [32].

It can be described using relation (1) with the introduction of a shielded value of the stress intensity factor range $\chi\,\Delta Keff$ as initially suggested by Suresh [33], with $0<\chi<1$ and χ depending on several factors as grain size, aged microstructure or anisotropy.

ii) Two environmentally assisted regimes operative in air and in moist atmospheres:

- Water vapor adsorption [5, 11, 20, 34, and 35] assisted stage II can be described with a relation derived [26, 29, and 35] from relation (1) as:

$$(da/dN)_{ad} = A/D^*[\Delta Keff/E]^4 = A[1/D^*_0 + \theta\,(1/D^*_{es} - 1/D^*_0)]\,(\Delta K_{eff}/E)^4 \qquad (2)$$

Adsorption is assumed to diminish the value of the cumulative displacement D*, in a manner similar to that in which adsorption diminishes the energy required to create a new fresh unit surface [26]. At high frequencies, the growth increment is rapid to the extent that no significant adsorption can take place ($\theta = 0$ and $D^* = D_0^*$ as in relation (1) for high vacuum). As the frequency decreases or/and da/dN decreases, more time becomes available for the molecules to form an adsorbed layer on the crack tip and thus the adsorption coverage increases ($0<\theta<1$) until reaching saturation ($\theta = 1$ and $D^* = D_{es}^*$) as in ambient air at conventional frequencies. Physical adsorption being a very rapid process, the kinetics of adsorption assisted propagation is controlled by the transport of water vapor molecules between the surrounding environment and the occluded crack tip environment. A reassessment of Wei's model has been done for the formulation of the crack impedance for a quasi-stationary crack and a molecular flow [35]. The evolutions of θ can be computed from the following equation:

$$\alpha S_o\theta/4F - \frac{1}{N_S\,V_a}\,\log(1-\theta) = \frac{P_O}{4\,N_O\,RT}\,t \qquad (10)$$

where α is the surface roughness parameter, S_0 the new fresh surface, F the Knudsen flow parameter, V_a the average molecular rate, N_S the number of stationary cycles, P_O the surrounding pressure, R the gas constant, T the temperature, and t the time.

- Hydrogen assisted stage II propagation [12, 13, 14, 20, 26] is described by a relation derived from the initial models of McClintock for ΔCTOD controlled propagation [36] as:

$$da/dN = B[\Delta K_{eff}^2/E\sigma] \qquad (3)$$

where B is a dimensionless coefficient and σ a strength parameter.

Critical conditions for the occurrence of hydrogen-assisted propagation which depends on hydrogen concentration into the process zone at the crack tip are as follows:

- the attainment of critical values for parameters controlling the number of molecules of water vapor required to create an instantaneous adsorbed mono-layer: partial pressure in the surrounding of the specimen, frequency, growth rate, R ratio.
- a sufficiently low stress intensity factor range in order to achieve a stationary crack and to localize the plastic deformation in slip bands at the crack tip;

In such conditions, the kinetics of environment fatigue crack propagation is controlled by crack tip surface chemical reaction to produce oxide-based compounds plus atomic hydrogen and diffusion of hydrogen in the process zone which means a reaction-controlled mechanism as described by Wei et al. [13-14]. To explain the action of hydrogen, some authors have shown by in-situ observations that Hydrogen induces an easier motion of the dislocations and a subsequently earlier rupture as compared to vacuum [37, 38]. This is also consistent with Beachem's theory [39] which suggests that instead Hydrogen locking dislocation in place, it unlocks them to multiply or move at reduced stresses' so that one might talk about enhanced plasticity. The exact controlling mechanism is still in discussion.

Finally, using a superposition model [14, 20, and 26], the following expression is given for a two steps environment-assisted propagation:

$$da/dN = (da/dN)_{ad} + (da/dN)_{H2} = A/D^* (\Delta K_{eff}/E)^4 + B[\Delta K_{eff}^2]/E\sigma \quad (4)$$

The present research on new generation Al alloys will provide new insights regarding alloy composition/microstructure as well as validation of the two steps model for environmentally assisted propagation.

EXPERIMENTAL

The alloys used in the present study were provided by Alcan with two new generation Al-Cu-Mg alloys in form of 40 mm thick plates of Al-Cu-Mg 2024A alloy in the T351 temper, and of Al-Cu-Mg 2022 alloy in the T351 and T851 tempers, and one third generation Al-Cu-Li alloy in form of 15.5mm thick plate of 2050 alloy in the T851 temper. The microstructures of both Al-Cu-Mg alloys are very similar and consist of grains elongated in the rolling direction (670x200x80 µm3). In naturally aged temper, the hardening precipitation consists in coherent Al-Cu Guinier-Preston (GP) zones mixed with Al-Cu-Mg GP(B) zones which are predominant in the 2024A alloy and few in the 2022 alloy.

	Chemical composition (%wt)	**Cu**	**Li**	**Mg**	**Mn**	**Ag**	**Si**	**Fe**	**Zn**	**Zr**	**Cr**	**Ti**
2022	*min*	4.5	-	0.1	0.15	-			0.05	-		
	max	5.5		0.45	0.5		0.15	0.2	0.3		0.05	0.15
8090	*min*	1.1	2.2	0.7		-				0.08		
	max	1.7	2.8	1.3	0.1		0.2	0.3	0.25	0.16	0.1	0.1
2050	*min*	3.2	0.7	0.2	0.2	0.2				0.06	-	-
	max	3.9	1.3	0.6	0.5	0.7	0.08	0.1	0.25	0.14		
2024A	*min*	3.7	-	1.2	0.15	-				-		
	max	4.5		1.5	0.8		0.15	0.2	0.25		0.1	0.15

Table 1: Chemical composition of the 2022, 8090, 2050 and 2024A alloys.

	Direction	**T°K**	**E** *(GPa)*	$\mathbf{R_{p0.2}}$ *(MPa)*	$\mathbf{R_m}$ *(MPa)*	**A%**	$\mathbf{K_{IC}}$ *(MPa.m$^{1/2}$)*	**d**
2022 T851	L-T	300	72	380	440	14	41	2.80
2022 T351	L-T	300	72	291	395	27	32	2.80
8090 T651	T-L	300	81	420	510	7	29	2.54
2050 T851	T-L	300	77	500	530	11	37	2.70
2024A T351	L-T	300	73	360	440	14	39	2.77
2024A T351	L-T	223	73	364	474	24	36	2.77

Table 2 : Main properties of the studied alloys.

The peak-aged heat treatment of the 2022 alloy is the standard temper designation T851 and consists of predominant incoherent θ' plates (Al2Cu) of about 100 nm length, and a few S (Al2CuMg) precipitates. The fibrous microstructure of the 2050T851 alloy consists of partially recrystallized grains strongly elongated in the rolling direction (1000x100x30 µm3), the hardening precipitation consisting mainly in non coherent T1 plates (Al_2CuLi) of about 100 nm length. For comparison purpose, results of previous studies on a second generation 8090 T651

Al-Li alloy [2, 3] are considered. This alloy, aged 12h at 190°C, consists of non recrystallized grains (50x10x10µm3) and fine recrystallized grains (10x10x6) µm3 and is characterized by coherent spherical δ'(Al_3Li), semi-coherent S' needles (Al_2CuMg) and non-coherent T1 plates.

Chemical compositions of the alloys are given in Table 1, and the main mechanical properties are presented in Table 2. Fatigue crack growth tests were performed on a servo hydraulic testing machine under load control. The loading signal was a sinusoidal waveform with a frequency of 35 Hz and a load ratio (R) of 0.1. The compact tension specimens were machined for a crack plane having orientation of table 2 with a width W of 50 mm and a thickness B of 10 mm. The crack length, a, was recorded with a traveling microscope. Threshold tests were performed using a load shedding procedure in accordance with the ASTM recommendation (E 647). After the attainment of growth rates da/dN lower than 10^{-10} m/cycle, a constant load test was performed at R=0.1 up to the near-failure domain. Crack closure measurements were carried out using the compliance method, by means of a capacitive gauge mounted at the mouth of the notch of the specimens [20].

For tests performed at low temperature, the temperature control of the specimen was achieved via four blocks of aluminum alloy fixed on the back of the specimens [40]. These blocks were cooled by means of silicon oil circulating from an external cooling source. The dew point in the atmosphere was controlled with a high precision hygrometer, the dry air being provided by an external apparatus. High vacuum tests were conducted at 223K and 300K inside the environmental chamber allowing a low pressure of $3x10^{-4}$ Pa.

FATIGUE CRACK PROPAGATION

Fig. 2 presents the results on the four alloys of the decreasing ΔK-constant R ratio experiments followed by increasing ΔK-constant load amplitude experiments in ambient air (Fig. 2a) and in high vacuum (Fig. 2b), each at a frequency f of 35 Hz.

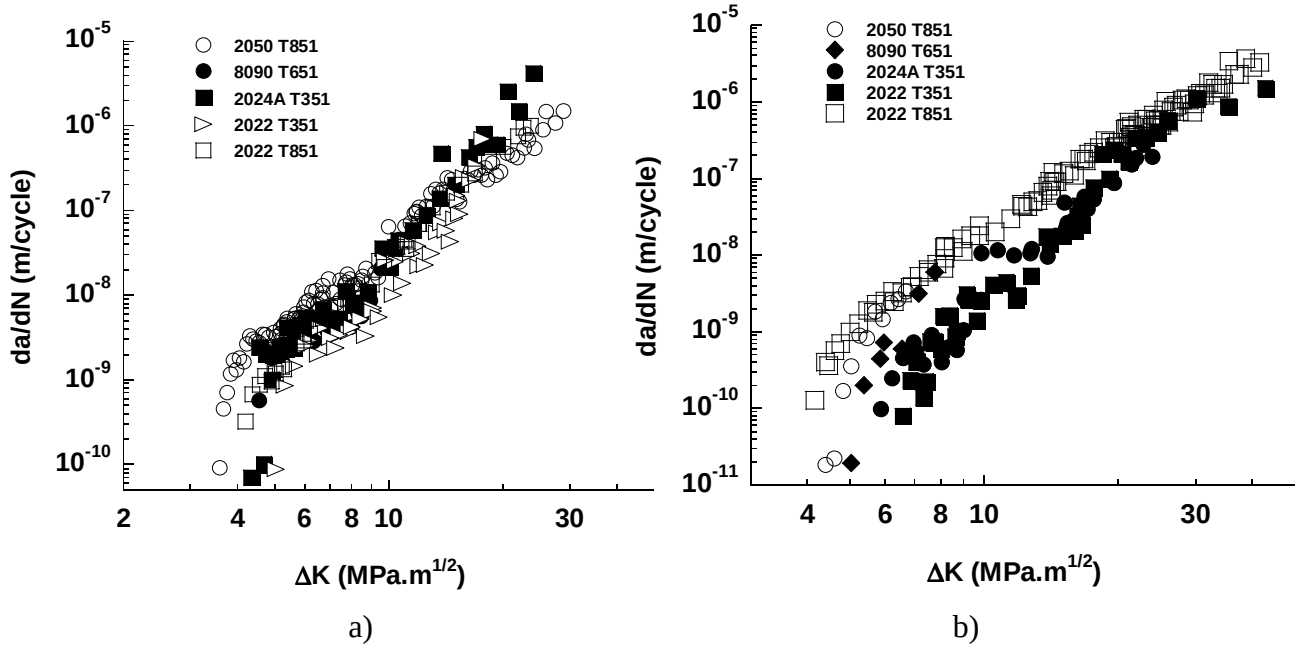

Figure 2: Comparison of fatigue crack propagation diagrams da/dN vs ΔK for the four studied alloys: a) ambient air; b) high vacuum.

In this experiments R is constantly equal to 0.1, and closure measurements were systematically performed to determine the stress intensity factor level for crack opening K_{op}.
With respect to the applied ΔK range, environment and microstructure are shown to strongly affect the fatigue crack growth rate (FCGR) as well for both peak-aged Al–Cu–Li alloys (2050 T851 and 8090 T651) as for the underaged Al–Cu-Mg 2024A T351 and 2022 T351. The "effective propagation" da/dN vs ΔK_{eff} with $\Delta K_{eff} = K_{max} - K_{op}$ are plotted in figure 3a for experiments conducted in ambient air and in figure 3b for high vacuum tests.

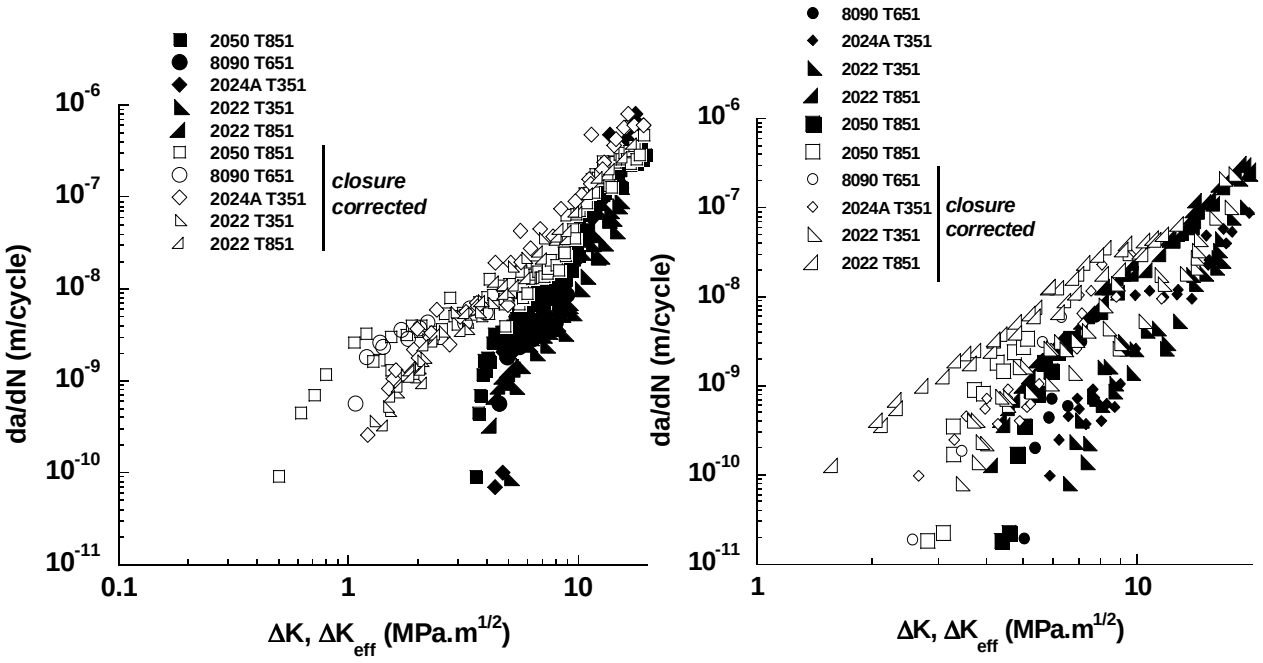

a) b)

Figure 3: Comparison of fatigue crack propagation diagrams da/dN vs ΔK and da/dN vs ΔK_{eff} for the four studied alloys: a) ambient air; b) high vacuum.

Da/dN for 2024AT351 and 2022 T351 and 8090 T651 are very similar as well in air as in high vacuum and also after closure correction. These two alloys present the best intrinsic resistance against crack propagation in high vacuum (figure 4a). The age hardening condition of the 2022 T851 does not strongly affect FCGR in air compared to vacuum, but the intrinsic resistance against crack propagation is slightly lower than that of the 2050 T851 but substantially lower than that of 2024A T351, 2022 T351 and 8090 T651. After closure correction (figure 4b), the two Li bearing alloys exhibit the best intrinsic resistance. In contrast, the behavior of the three alloys (2024A, 2022 and 8090) in air is very similar even after closure correction while the 2050 alloy shows the highest sensitivity to air environment in the near threshold domain.

Globally it can be concluded that under aging on Al-Cu-Mg alloy and peak aging on Al-Cu-Li alloys causes a dramatic loss in FCP intrinsic resistance in air compared to high vacuum which is not observed on the peak aged Al-Cu-Mg 2022 T851. So the latter alloy presents the poorest intrinsic resistance in high vacuum but, in contrast, it presents the best resistance in air. This trend is consistent with data on the effect of aging on FCP recently published by Gangloff et al. (31) supporting that in conventional alloys under aging effect on da/dN is dramatic for ultra-high vacuum, but modest for fatigue in water vapor atmosphere or in air.
The crack growth rate trends to correlate with fatigue crack morphology changes, as summarized by the scanning electron fractographs in Figs. 5, 6 and 7. For samples cracked in vacuum, both

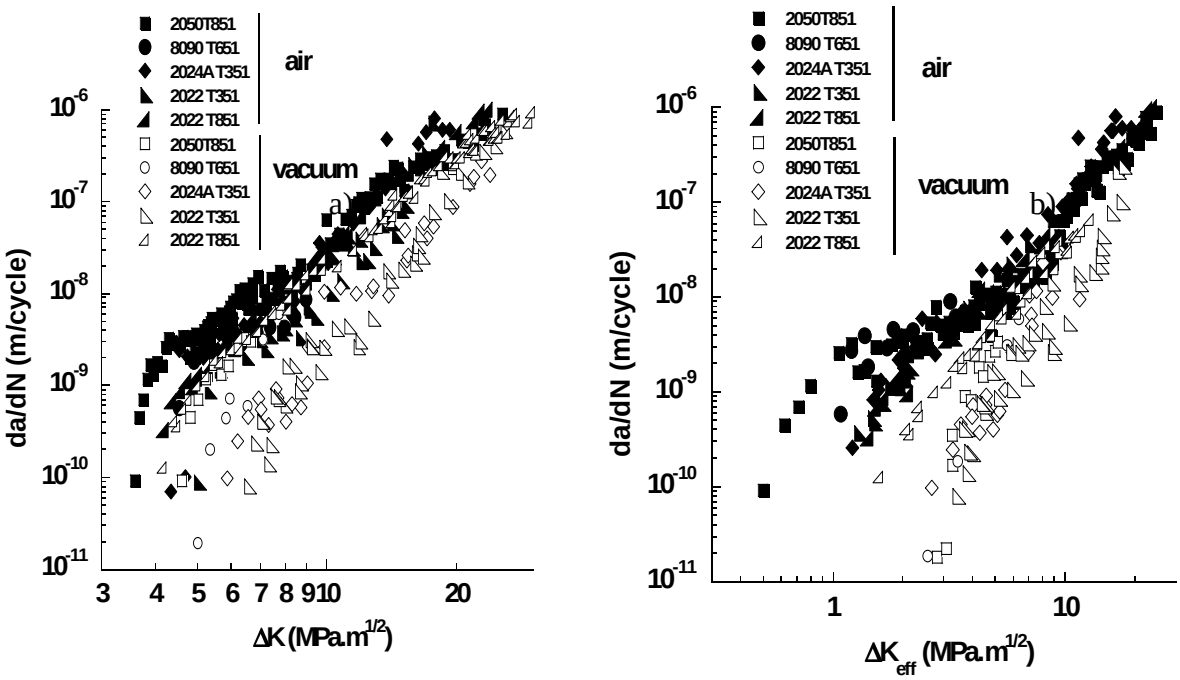

Figure 4: Influence of ambient environment on fatigue crack propagation: a) da/dN vs ΔK, and b) da/dN vs ΔK_{eff}.

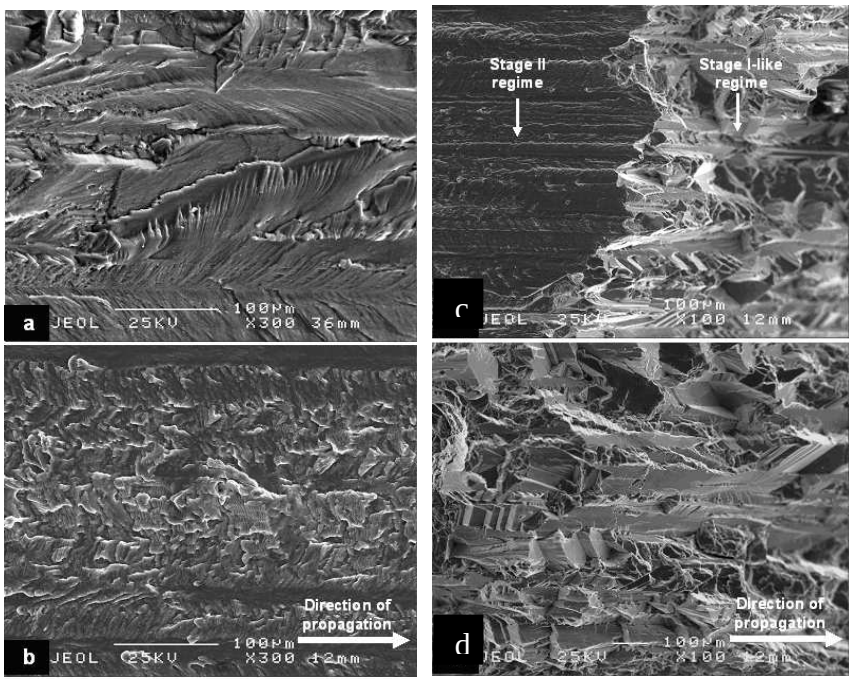

Figure 5: SEM micrographs of 2050 T851. a) ambient air at ΔK = 6 MPa.m$^{1/2}$; b) vacuum at ΔK = 6 MPa.m$^{1/2}$; c) Transition stage II to stage I-like at ΔK = 5 MPa.m$^{1/2}$; d) stage I like at ΔK = 4.5 MPa.m$^{1/2}$

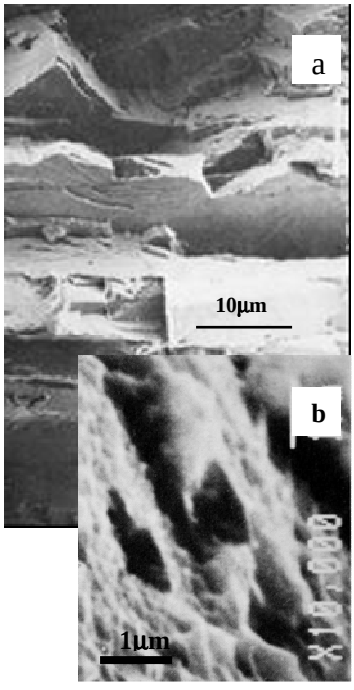

Figure 6: a) SEM micrographs of 8090 T651in high vacuum; b) (111) facet identified from triangular etch pits.

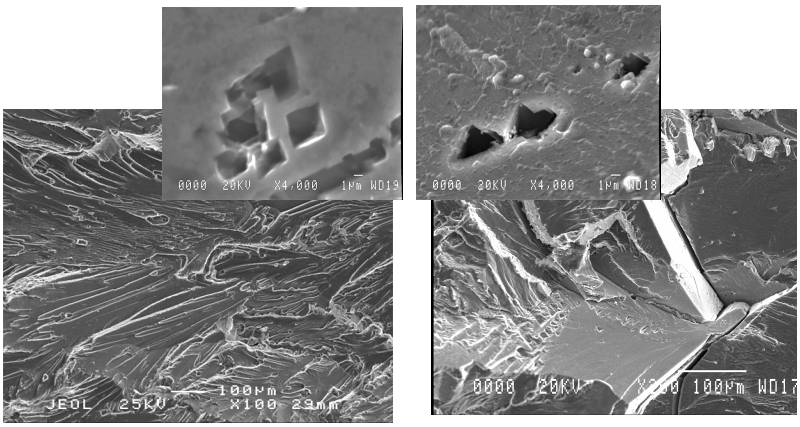

a) b)

Figure 7: SEM fracture surface morphology in high vacuum: a) 2022 T851: stage II crack path with zoom on square etch pits for (100) or (110) propagation plane; b) 2024A T351: stage I like crack path with zoom on triangular etch pits for (111) facets.

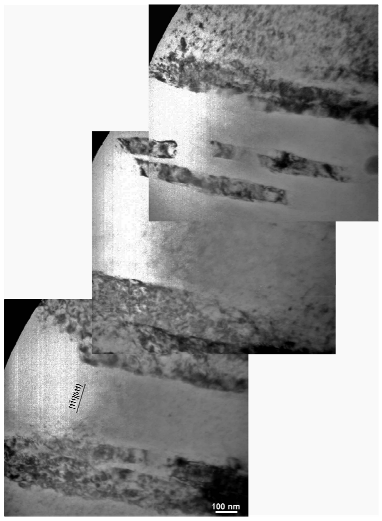

Fig. 8: MET observations of (111) slip bands made on a sample extracted just under the stage I-like fracture surface of 2024A T351 as in figure 7b.

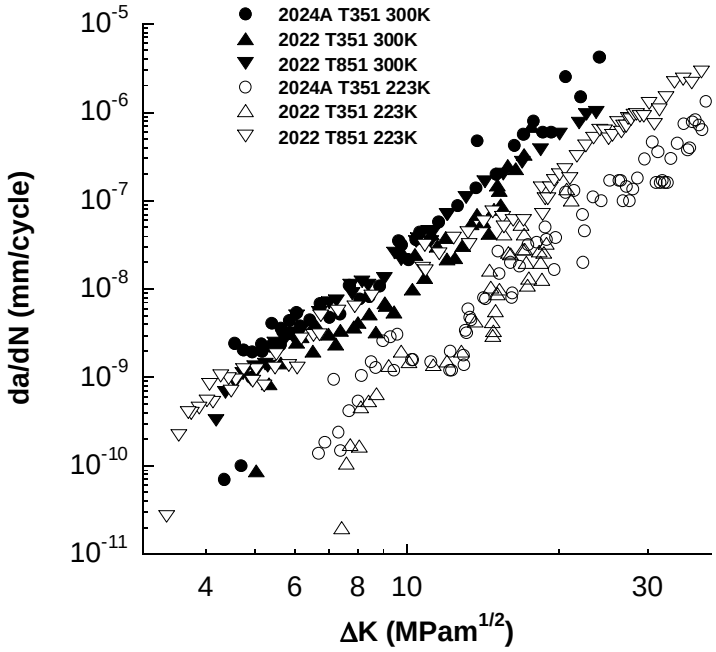

Figure 9: Influence of temperature on the crack propagation rate: ambient air (300K) and cold air (223) at R=0.1 and 35Hz.

peak aged Al-Cu-Li exhibit faceted and microscopically tortuous near threshold fatigue crack paths, as shown in Fig. 5d and 6, comparable to that of 2024A T351 (fig.7b) and 2022 T351.

The crystallographic facets have been identified in all cases of crystallographic propagation path as (111) or near-(111) surface facets associated with slip-band cracking [20, 21, 22, 29, 31, 40] as illustrated with triangular etch pits on for 8090 T651 (figure 6b) and 2024A T351 (figure 7b). This can be explained mechanistically in terms of slip localization induced by shearable precipitates (δ' and δ' +T1) in Al–Cu–Li alloy and solute clusters in Al–Cu–Mg; this deformation behavior correlates with good FCGR resistance resulting from enhanced grain boundary barrier effect for slip bands, and also crack branching and deviation [20, 29, 32, 35]. TEM observations performed on thin foils extracted within the fracture surface of a 2024A T351 specimen fatigue in high vacuum (Fig. 8) illustrate (111) dislocations bands in accordance with a localization of the plastic deformation within single slip bands orientation in each individual grain for a crack grown at sufficiently low ΔK range.

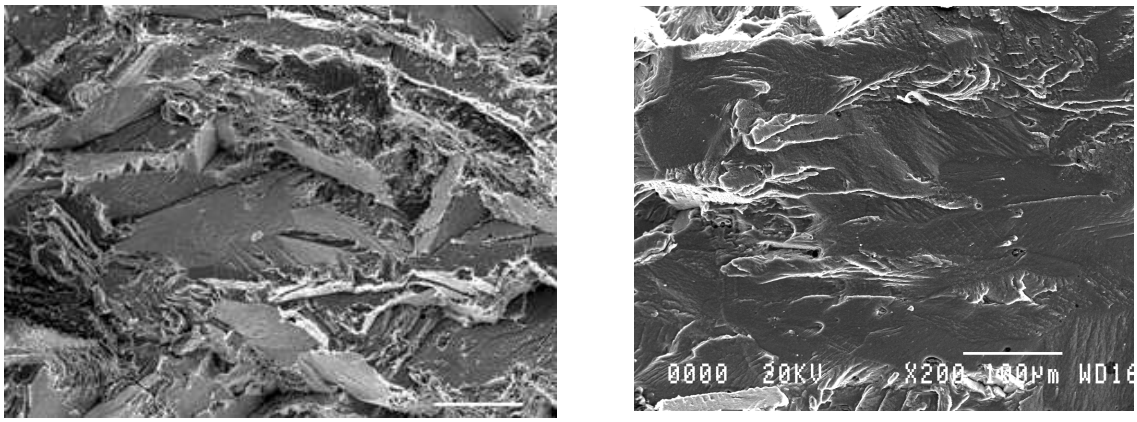

a) b)

Figure 10: a) 2024A T351: crystallographic crack path in dry air at 223K;
b) 2022 T851: stage II crack path in air at 300K.

The Fatigue Crack Growth rates da/dN in ambient air (300K) and in cold air (223K) are plotted in figure 9 with respect to the ΔK range for 2024A T351 alloy. The curves obtained at 300K for the three alloys are quite similar. At 223K, a marked effect of temperature for the T351 temper consists in a substantial reduction of the crack growth rates. SEM observations of the fracture surfaces of figure 10a show a rough crystallographic crack path associated to a retarded crack propagation in the naturally aged alloy in contrast with the flat crack path in the peak aged temper T851 (figure 10b), which is comparable to that obtained at room temperature. The da/dN vs ΔK_{eff} diagram of figure 11a compares the crack propagation data at room temperature and 223K in air and vacuum for the 2024A T351. Changing environment condition from ambient air to dry cold air induces an abrupt change in the fracture surface morphology of underaged Al-Cu-Mg alloys as shown in figure 11b for 2024A T351. The straight lines in figure 11a correspond to the different regimes of the modeling framework of the background section.

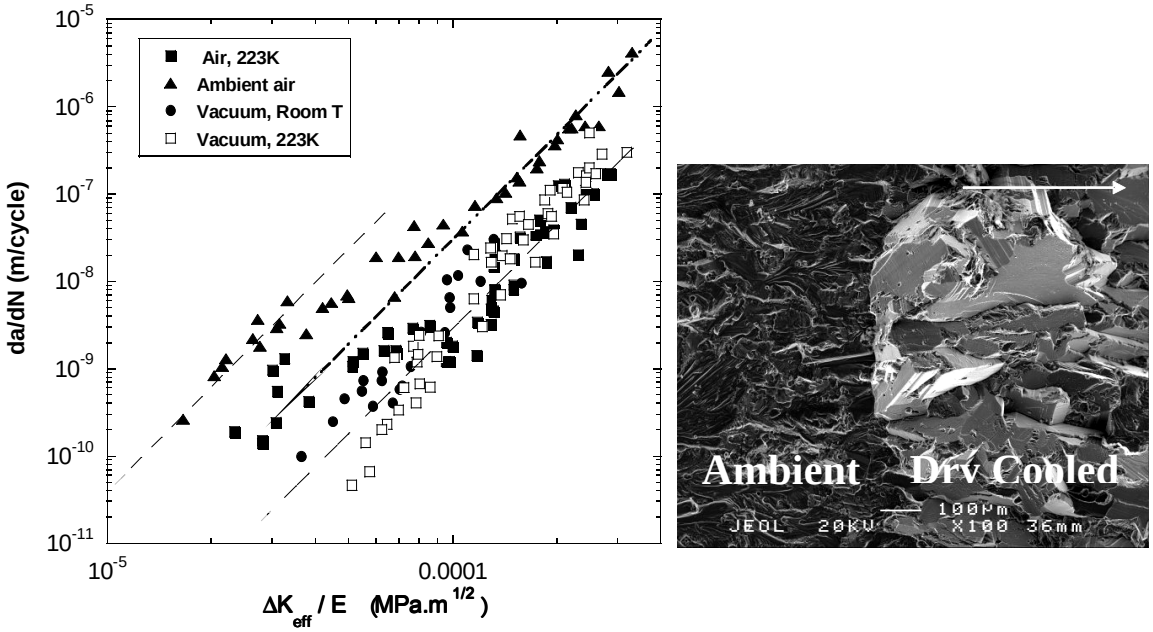

a) b)

Fig. 11: Influence temperature and air humidity on da/dN in 2024AT351 [26]: a) da/dN vs ΔKeff/E in air and high vacuum at 223K and room T; b) SEM observations of fracture surface when environment is changed from ambient air to dry air at 223K.

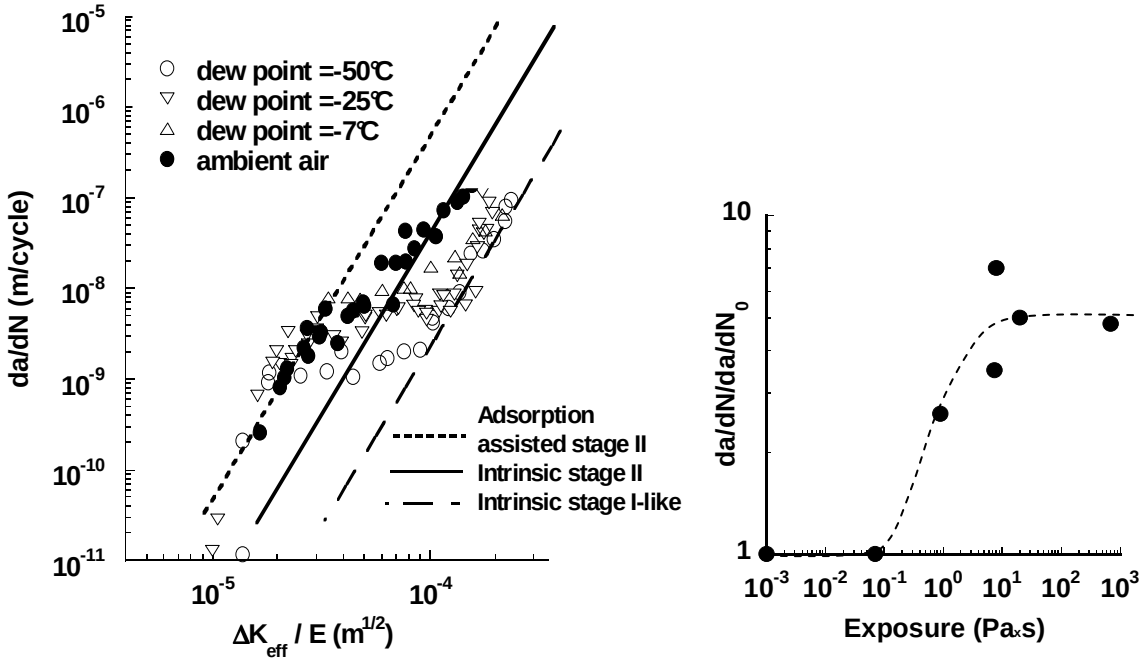

a) b)

Figure 12: Influence of air dryness (water vapor exposure) on da/dN for 2024A T351:
a) da/dN vs ΔK; b) $(da/dN)_{dewpoint}/(da/dN_{vacuum})$.

The crack propagation in air at room temperature corresponds typically to the intrinsic stage II regime at mid ΔK with a transition to the adsorption assisted regime in the near threshold domain. The crack path is similar to that of figure 10b. In high vacuum at both temperatures and in cold air the crystallographic stage I like regime prevails. The atmospheric moisture at room temperature (about 1.7kPa of water vapor) contribute to the activation of secondary slip planes, the adsorbed water vapor molecule reducing drastically the slip reversibility in contrast with easy slip reversibility favored by slip localization in underaged microstructure in high vacuum or in dry air at 223K when water vapor exposure is highly reduced. In the peak aged structure of 2022 T851 S' precipitates from artificial aging are not shearable and planar bands of dislocation structure do not form whatever temperature and air dryness. A similar effect of homogeneous slip favoring bypassing of precipitates and inducing faceted crack path is reported for vacuum fatigue crack growth in 7075-T651 compared to the overaged (T7351) condition [17, 20].

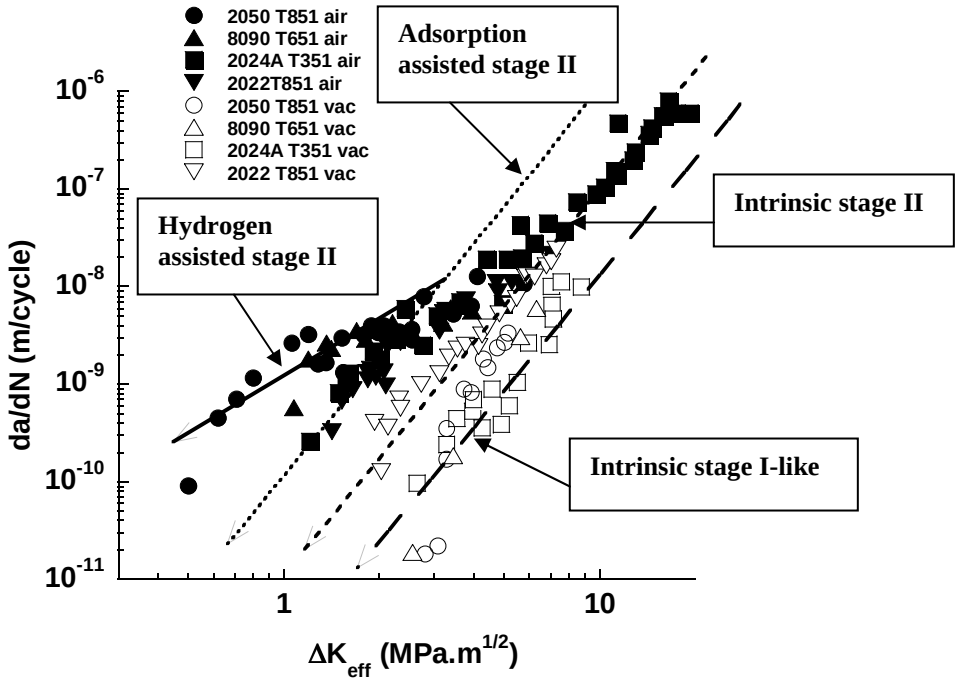

Figure 13: Experimental data confronted to modeling: intrinsic propagation in high vacuum (stage II and stage I-like), water vapor and hydrogen assisted stage II in air.

As mentioned in the background section, water vapor molecules are the active species of ambient air. The crack surface of each alloy and aging condition exhibits similar morphology in the presence of water vapor, with areas of flat-facet and step-like

features (figures 5 and 7a). Detailed analysis of such features [17, 31, 40] established that there is a complex array of surface orientations that span from (100) to (110) as illustrated in figure 7b for 2022 T851.

The influence of exposure to water vapor is presented in figure 12 illustrating the influence of the partial pressure in air on the fatigue crack propagation rate in the 2024A T351 alloy. Increased partial pressure induces accelerated propagation (figure 12a) for exposure ranging in a critical interval above 10^{-2} Pa.s as illustrated in figure 12b for $\Delta K=7MPam^{1/2}$. This critical exposure is comparable to that determined by Gangloff et al. [31] for comparable Al-Cu-Mg and Al-Cu-Li alloys. These results substantiate the speculative modeling of adsorption assistance.

In figure 13, the experimental data in air and in high vacuum after closure correction are confronted to the different regimes described in the background section. In the near threshold domain, the crystallographic propagation in high vacuum in 2050, 8090 and 2024A is adequately described in term of the stage I like regime, while the peak aged 2022 is in accordance with the intrinsic stage II regime. At higher ΔKeff range, in the intermediate so-called Paris regime, the intrinsic stage II regime prevails for the four materials.

In air, for growth rates slower than 10^{-8} m/cycle ($\Delta Keff < 3MPa.m^{1/2}$), adsorption assisted stage II is operative for both underaged and peakaged Al-Cu-Mg alloys, in contrast with both Al-Cu-Li alloys that are governed by a hydrogen assisted stage II. In the Paris regime, water vapor assistance vanishes in all cases, and the intrinsic stage II regime is progressively reached.

Finally, it comes out that the peak aged Li bearing alloys behave as underaged Al-Cu-Mg alloys in high vacuum with the highest resistance against crack propagation, in contrast with a dramatic lost of resistance due to their susceptibility to water vapor. In the domain of moderate ΔK the Al-Cu-Li and Al-Cu-Mg alloys present a similar behavior in ambient air. In the near threshold domain and at low R ratio, a more substantial contribution of crack closure (particularly the 8090 alloy) leads to very similar near threshold behavior as that of Al-Cu-Mg alloys even if after closure correction or in absence of closure at higher R ratio, the Li bearing alloys present a poorer resistance because of their sensitivity to hydrogen assistance.

Conclusions

The following conclusions can be drawn relevant to fatigue crack propagation Al–Cu–Li (2050 T851 and 8090 T651 in comparison to Al–Cu–Mg (2024A T351, 2022 T351 and 2022 T851) :

1. The fatigue crack growth rate evolution with respect to ΔK in ambient air is substantially accelerated in comparison to high vacuum whatever the microstructure and the alloy composition. This acceleration is governed by the exposure to atmosphere water vapor. At exposure to water vapor lower than 10^{-2}

Pa.s as in dry cold air at 223K at 35Hz, the influence of environment vanishes and the behavior is similar to that in vacuum.

2. Crack growth resistance in absence of atmosphere assistance can be substantially improved by underaged microstructure but this role of microstructure is inhibited by the 1.7 kPa of water vapor of ambient air.
3. Crack closure does not account for environment effect nor microstructure influence in high vacuum.
4. In high vacuum slip morphology controls da/dN and identical and slow growth rates of a stage I-like regime are produced for shearable precipitate in Al-Cu-Li alloys or solute GP cluster structures in underaged Al-Cu-Mg, that promote heterogeneous slip-band formation and (111)-faceted cracking; a similar mechanism controls da/dN is cold dry air for underaged Al-Cu-Mg when exposure to water vapor is restricted. In contrast a ductile featureless flat stage II morphology is prevailing in high vacuum with much faster da/dN for the peak aged Al-Cu-Mg 2022 T851;
5. The damage tolerance of Al-Cu-Li in ambient air is comparable to the reference damage tolerance of the Al-Cu-Mg alloys and results from a substantial contribution of crack closure for low R ratio (R=0.1) that equilibrates the higher sensitivity of Al-Cu-Li alloys to hydrogen assistance;

REFERENCES

1. E. P. Dahlberg, *Trans. A.S.M.* 58 (1965), pp. 46-53.
2. H. Ishii, J. Weertman, *Scripta Met.* 3 (1969), pp. 229-235.
3. J. S. Enochs and O. Devereux, *Metall Trans,* 6A (1975), pp. 391-397.
4. A. Hartman, *International journal of fracture mechanics,* 1 (1965), pp. 167-188.
5. F. J. Bradshaw and C. Wheeler, *Applied Materials Research* (1966)**,** pp. 112-120.
6. R. P. Wei, *Engineering Fracture Mechanics,* 1 (1968), pp.633-651.
7. D. A. Meyn, *Trans ASM,* 61 (1968), pp.52-61.
8. D. Broeck, A. Hartman and A. Nederveen, *NLR Report TR 71032 U* (1971), pp. 543-622.
9. R. J. H. Wanhill, *Metallurgical Transactions,* 6A (1975), pp. 1587-1596.
10. Lindigkeit, A. Gysler and G. Lutjering, *Metall Trans,* 12A (1981), pp. 1613-1619.
11. B. Bouchet, J. de Fouquet and M. Aguillon, *Acta Met,* 23 (1975), pp. 1325-1336.
12. B. R. Kirby and C. J. Beevers, *Fat Engng Mater Struct,* 1 (1979), pp. 203-215.
13. R. P. Wei, *Engineering Fracture Mechanics,* 1 (1968), pp. 633-651.
14. R. P. Wei and G. W. Simmons, *Int. J. Fract.,* 17 (1981), pp. 235-247.
15. C. Bowles and J. Schijve, *ASTM STP 811* (1983), pp. 400-426.
16. J. Lankford and D. L. Davidson, *Acta metall,* 31 (1983), 1273-1284.
17. E. A. Starke Jr, F. S. Lin, R. T. Chen and H. C. Heikkenen, *Fatigue Crack Growth Threshold Concepts*, Metallurgical Society of AIME pub.(1984), pp. 43-62.
18. J.-P. Bailon, M. El Boujdani and J. I. Dickson, *Fatigue Crack Growth Threshold Concepts*, Metallurgical Society of AIME pub. (1984), pp. 63-82.

19. S. Suresh and R. O. Ritchie, *Fatigue Crack Growth Threshold Concepts*, Metallurgical Society of AIME pub. (1984), pp. 227-261.
20. J. Petit, *Fatigue Crack Growth Threshold Concepts*, Metallurgical Society of AIME pub. (1984), pp. 3-24.
21. N. Ranganathan, S.Q. Li, J.P. Baïlon and J. Petit, *Materials Science and Engineering*, A187 (1994) 37-42.
22. J. Petit and A. Zeghloul, *ASTM-STP 1049* (1990), pp. 334-346.
23. R. S. Piascik and R. P. Gangloff, *Metall Trans,* 22A, (1991), pp. 2415-2428.
24. R. S. Piascik and R. P. Gangloff, *Metall Trans,* 22A, (1991), pp. 2751-2762.
25. J. Ruiz and M. Elices, *Acta Mater,* 45 (1997), pp. 281-293.
26. J. Petit, G. Hénaff and C. Sarrazin-Baudoux, *ASTM STP 1372* (2000), pp. 3-30.
27. N. Ranganathan, M. Quintard, J. Petit and J. de Fouquet, *ASTM STP 811* (1990), pp. 374-390.
28. H. J. Gudladt and J. Petit, *Scripta Metall & Mater,* 25 (1991), pp. 2507-2512.
29. J. Petit, G. Hénaff and C. Sarrazin-Baudoux, , *Comprehensive Structural Integrity*, Vol. 6, *Environmentally-assisted Fracture,* J. Petit and P. Scott eds., (2003), p. 211.
30. J. Petit and G. Hénaff, *Proceedings of Proceedings of Fatigue 93,* EMAS, (1993), pp. 503-512
31. Y. Ro, S.R. Agnew, G.H.Bray and R.P. Gangloff, Material Science and Engng. A 468-470 (2007), 88-97.
32. K. J. Miller and E. R. De Los Rios, *The Behaviour of Short Fatigue Cracks,* Mechanical Engineering Publications Limited, London, U.-K. (1986).
33. S. Suresh, *Metall. Trans.,* 16 **(**1985), pp. 249-260.
34. S. P. Lynch, *ASTM STP 675,* (1978), pp. 174-213.
35. G. Henaff, K. Marchal and J. Petit, *Acta Metall. Mater.,* 43 (1995), pp. 2931-2942.
36. F. A. McClintock, *Proc. Fracture of Solids,* Maple Valley WA, (1963), pp. 65-102.
37. T. Tabata and H. K. Birnbaum, *Scripta Metall.,* 17 **(**1984), 947-950.
38. H. K. Birnbaum and P. Sofronis, *Mater. Sci. and Engng.* 176 A (1994), pp. 191-202.
39. C. D. Beachem, *Metall Trans,* 3 **(**1972), pp. 437-451.
40. C. Gasqueres, C. Sarrazin-Baudoux and J. Petit Fatigue in: proc. FCP 2006, A. Carpintieri ed., Parma, Italy.
41. R. O. Ritchie, D. L. Davidson, B. L. Boyce, J. P. Campbell and O. Roder, *Fatigue Fract Eng Mater Struc,* 22 (1999), pp. 621-631
42. 101. S. Suresh, *Metall Trans,* 16A (1985), 249-260.
43. 102. K. J. Miller and E. R. De Los Rios, *The Behaviour of Short Fatigue Cracks,* Mechanical Engineering Publications Limited, London, U.-K. (1986).